4. SITE 864[1]

Shipboard Scientific Party[2]

HOLE 864A

Date occupied: 30 January 1992

Date departed: 26 February 1992

Time on hole: 27 days, 16 hr, 30 min

Position: 9°30.852′N, 104°14.658′E

Bottom felt (rig floor; m, drill-pipe measurement): 2581.7

Distance between rig floor and sea level (m): 10.50

Water depth (drill-pipe measurement from sea level, m): 2571.2

Total depth (rig floor; m): 2596.7

Penetration (m): 15.0

Number of cores (including cores with no recovery): 5

Total length of cored section (m): 8.60

Total core recovered (m): 9.50

Core recovery (%): 110

Hard rock:
Depth (mbsf): 0–15.0
Nature: basalt
Measured velocity (km/s): 4.8–5.1

Basement:
Depth (mbsf): 0–15.0
Nature: basalt
Measured velocity (km/s): 4.8

Drill below core (m): 15.00

Comments: Recovery percentage meaningless due to definition of junk-basket samples as core.

HOLE 864B

Date occupied: 26 February 1992

Date departed: 4 March 1992

Time on hole: 6 days, 7 hr, 30 min

Position: 9°30.852′N, 104°14.658′E

Bottom felt (rig floor; m, drill-pipe measurement): 2582.9

Distance between rig floor and sea level (m): 10.50

Water depth (drill-pipe measurement from sea level, m): 2572.4

Total depth (rig floor; m): 2590.2

Penetration (m): 7.3

Number of cores (including cores with no recovery): 2

Total length of cored section (m): 3.10

Total core recovered (m): 0.14

Core recovery (%): 5

Hard rock:
Depth (mbsf): 0–3.0
Nature: basalt
Measured velocity (km/s): 4.1–4.3

Basement:
Depth (mbsf): 0–3.0
Nature: basalt
Measured velocity (km/s): 4.1–4.3

Drill below core (m): 7.20

HOLE 864C

Date occupied: 4 March 1992

Date departed: 6 March 1992

Time on hole: 2 days, 12 hr, 30 min

Position: 9°30.852′N, 104°14.658′E

Bottom felt (rig floor; m, drill-pipe measurement): 2582.9

Distance between rig floor and sea level (m): 10.50

Water depth (drill-pipe measurement from sea level, m): 2572.4

Total depth (rig floor; m): 2589.7

Penetration (m): 6.80

Number of cores (including cores with no recovery): 0

Total length of cored section (m): 0.00

Total core recovered (m): 0.00

Core recovery (%): 0

Drill below core (m): 6.80

Principal results: Site 864 was located on a flat, relatively unfissured lava flow flooring the axial summit caldera of the East Pacific Rise (EPR) at about 9°30′N. Three holes were drilled, and two (Holes 864A and 864B) yielded samples in the form of angular fragments recovered by the diamond coring system (DCS), miscellaneous junk-basket and bit-recovery samples, and a cylindrical wash core cut by the DCS (Table 1). On the basis of geochemical and petrographic results, two lithologic units have been identified. Unit 1 consists of massive glassy to fine-grained aphyric basalt. Recovered fragments commonly show thin (<1 cm thick) glassy margins grading into microcrystalline interiors; some angular fragments consist entirely of pure glass, whereas others are entirely crystalline. Drilling conditions and the nature and chemistry of the recovered material indicate that Unit 1 consists of a 2- to 3-m-thick massive flow, underlain by several meters of glassy lobate or sheet flows (Fig. 1), all likely emplaced during a single eruptive event. An additional massive flow of unknown thickness, possibly sampled by junk-basket samples, may underlie the lobate and sheet flows; the total thickness of Unit 1 unknown but is likely to be less than 6.6 m. Phenocrysts in Unit 1 samples are sparse (<1%) and consist of euhedral, prismatic plagioclase (up to 1.5 mm in length) and rare clinopyroxene. The groundmass consists of varying proportions of glass, cryptocrystalline mesostasis, microcrystalline to fined-grained plagioclase, olivine, clinopyroxene, titanomagnetite, and small (5–10 microns, or μm) Fe-sulfide globules. Groundmass textures are consistent with differing rates of quench crystallization and cover a complete spectrum from glassy and spherulitic to

[1] Storms, M.A., Batiza, R., et al., 1993. *Proc. ODP, Init. Repts.*, 142: College Station, TX (Ocean Drilling Program).
[2] Shipboard Scientific Party is as given in the list of participants preceding the contents.

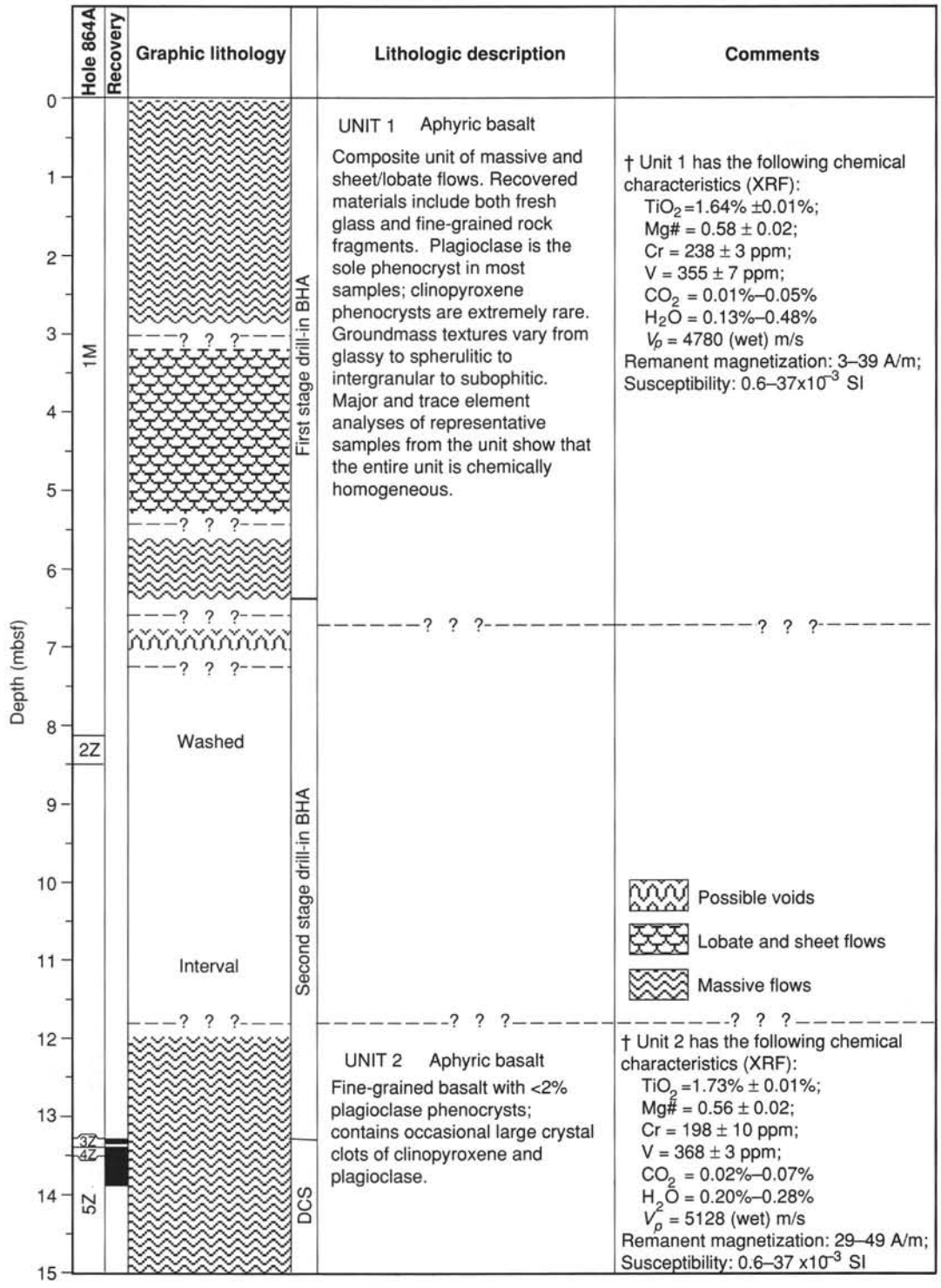

Figure 1. Inferred stratigraphy at Site 864 from drilling parameters and petrological observations. Unit and lithological boundaries are highly uncertain. (BHA = bottom-hole assembly)

microlitic to fine-grained intergranular, sometimes with subophitic intergrowths of plagioclase and clinopyroxene. Vesicularity is low (0% to 5%). In general, samples are quite fresh, but microcracks and fracture surfaces of some fragments exhibit thin coatings of secondary precipitates, including opaline silica and cryptocrystalline quartz, Fe-oxyhydroxide minerals, minor pyrite and chalcopyrite, Cu-sulfate?, and possible clay minerals.

Unit II is a massive, microcrystalline to fine-grained, aphyric to slightly plagioclase phyric basalt. It is separated from Unit 1 by an interval of no recovery during drilling and washing (Fig. 1), and represents a thick, jointed lava flow or dike of unknown thickness recovered from an interval from 11.8 to 15.0 meters below seafloor (mbsf). One recovered fragment displays well-developed polygonal jointing. Phenocrysts are sparse (up to 2%) and consist of euhedral, tabular to prismatic plagioclase crystals (<2.1 mm) and rare olivine. Occasional, large (up to 1 cm diameter), coarse-grained crystal clots of euhedral, prismatic clinopyroxene and plagioclase are present. Groundmass mineralogy and textures are identical to Unit I.

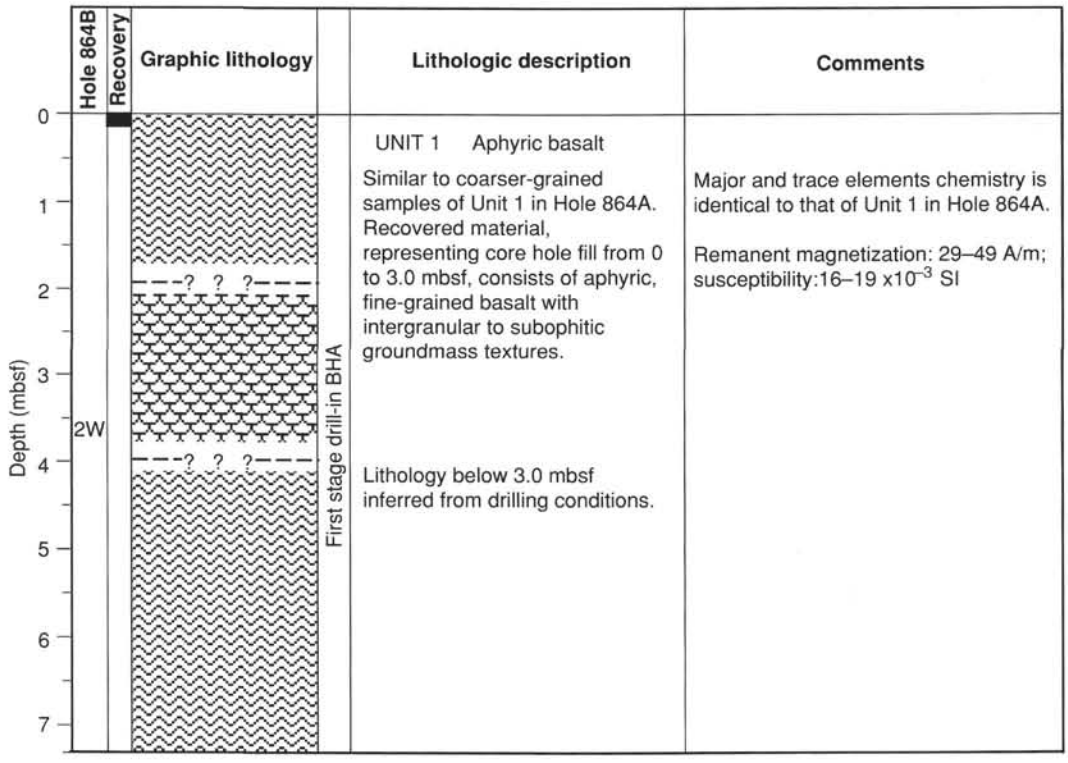

Figure 1 (continued).

Vesicularity is low, but is generally higher than in Unit 1 (0% to 6%). All samples are fresh but traces of hydrothermal alteration are occasionally found as thin coatings of opaline silica, cryptocrystalline quartz, and Fe-oxyhydroxide minerals. Rust-colored clay minerals rarely occur as partial vesicle fillings.

Representative whole-rock and picked glass samples from Unit 1 (n = 13) and whole-rock samples from Unit 2 (n = 2) were analyzed for major and trace elements by X-ray fluorescence. Within each unit, samples yielded identical values within analytical precision. Units 1 and 2 are compositionally very similar, relatively evolved normal-type mid-ocean ridge basalt (N-MORB), with average Mg/(Mg + Fe^{2+}) of 0.58 and 0.56, respectively. Compared to Unit 1, Unit 2 is characterized by slightly higher TiO_2 (1.78% vs. 1.64%), Na_2O (2.63% vs. 2.55%), Y (40 vs. 36 ppm), and V (369 vs. 355 ppm), and by slightly lower Al_2O_3 (14.03% vs. 14.30%), CaO (11.45% vs. 11.71%), and Cr (188 vs. 238 ppm). Nb, K_2O, and P_2O_5 are low in both units (3 ppm, 0.14%, 0.11%–0.12%, respectively), and CO_2 and H_2O contents of glass from Unit 1 ranged from 0.01% to 0.04% and 0.13% to 0.23%, respectively. Units 1 and 2 were derived from parental lavas similar to those that produced other N-MORB from this portion of the EPR, with the minor differences between the two Leg 142 units consistent with Unit 2 having undergone slightly more low-pressure fractionation of olivine, plagioclase, and clinopyroxene than Unit 1.

Grain densities of Leg 142 basalt samples ranged from 2.99 to 3.02 g/cm^3, with wet-bulk densities of 2.94 to 2.99 g/cm^3 indicating porosities of 1.8% to 2.1%. Compressional wave velocities of these basalts were low for basalts, ranging between 4.1 to 5.1 km/second (s) (seawater-saturated) and 3.0 to 4.1 km/s (dry). The large differences between wet and dry velocities exhibited by most samples tested implies that a significant part of the rock porosity consists of microcracks. The mean magnetic susceptibility of the basalts (0.015 SI units) is comparable to that of other ocean-ridge basalts, and shows a great range (0.00066 to 0.033 SI units). The natural remanent magnetization (NRM) of the samples is also broad (0.17 to 0.49 A/m), with the lowest values measured from glassy samples. Magnetic and thermal coercivities of the samples are low, consistent with multidomain Ti-rich magnetite being the dominant carrier of the NRM.

IGNEOUS PETROLOGY

Introduction

Site 864 is located on a flat, relatively unfissured lava flow erupted within the axial summit depression of the East Pacific Rise at 9°30′N latitude. Igneous rocks were recovered from two closely spaced holes (Holes 864A and 864B) which penetrated basement to depths of 15.0 and 7.4 mbsf, respectively. Based on drilling parameters and sample recoveries from both holes, a general stratigraphy for the drill site has been established (Fig. 1). With depth, this stratigraphy consists of a thick (2–3 m) massive lava flow, a several-meter-thick zone of thin sheet and/or lobate lava flows possibly underlain by an additional massive lava flow, a gap of several meters where no core was recovered, and another massive flow or dike of undetermined thickness. Corresponding sample recoveries include (see Fig. 1): (1) the uppermost interlayered massive lava flows and thin sheet- and/or lobate-flows (Cores 142-864A-1M and 142-864B-2W); and (2) the lowermost massive unit (Core 142-864A-3Z to -5Z).

Based on identical geochemical characteristics, the uppermost interlayered massive lava flows and thin sheet and/or lobate flows are believed to represent one eruptive event and have been placed within a single lithologic unit (Unit 1). Samples from the lowermost massive lava flow are petrographically and geochemically distinct and have been placed in a separate unit (Unit 2). Both units are typical of N-MORB. Below, their general lithologic, petrographic, and geochemical characteristics are discussed in detail.

Lithology and Petrography

All samples from both Units 1 and 2 are fresh, aphyric to sparsely phyric, slightly vesicular (up to 6%), glassy to fine-grained crystalline basalts. Many fragments display varying degrees of fracturing and breakage formed during drilling and milling while some show evidence for preexisting jointing formed during cooling. Minor hy-

Table 1. Coring summary, Site 864.

Core	Date (1992)	Time (local)	Depth (mbsf)	Length cored (m)	Length recovered (m)	Recovery (%)
142-864A-						
1M	7 Jan.	0700	0.0–6.6	6.6	9.00	136.0
2Z	17 Feb.	1900	8.2–8.5	0.3	0.00	0.0
3Z	22 Feb.	0300	13.3–13.4	0.1	0.06	60.0
4Z	23 Feb.	1330	13.4–13.5	0.1	0.11	110.0
5Z	24 Feb.	0650	13.5–15.0	1.5	0.33	22.0
			Coring totals	8.6	9.50	110.0
142-864B-						
1R	29 Feb.	2135	1.0–1.1	0.1	0.00	0.0
2W	1 Mar.	0715	0.0–3.0	3.0	0.14	Wash core
			Coring totals	0.1	0.00	0.0
			Washing totals	3.0	0.14	
			Combined totals	3.1	0.14	

drothermal alteration and traces of secondary sulfide mineralization are present in many pieces recovered within the sampled interval. Plagioclase is a ubiquitous phenocryst phase which is very rarely joined by clinopyroxene or olivine. Two samples from Unit 2 contain large (up to 1 cm diameter), coarse-grained clots of intergrown plagioclase and clinopyroxene. Groundmass textures are consistent with differing rates of quench crystallization and display a complete spectrum from (1) entirely glass (glassy), to (2) glass and noncoalesced spherules with or without minor microlites (glassy to spherulitic), to (3) coalesced spherules with abundant microlites (spherulitic or variolitic to microlitic), to (4) interconnected microlites set in a dark, cryptocrystalline mesostasis (intersertal), to finally (5) interconnected, fine-grained crystals often displaying an intergranular to subophitic texture (see Figs. 3 through 6 in the "Explanatory Notes" chapter, this volume).

Unit 1: Aphyric Basalt

Rock fragments assigned to Unit 1 were recovered from Holes 864A (Core 142-864A-1M) and 864B (Core 142-864B-2W). Individual fragments (Fig. 2) are all very fresh, angular to subrounded (due to drilling), and range in size from less than 1 cm to at most 5 cm in diameter. All pieces are massive, slightly vesicular, and display a complete range in texture from glassy to microcrystalline to fine-grained crystalline. Some fragments show thin (less than 1 cm thick) glassy margins grading into microcrystalline interiors. Glassy samples usually contain spherules, often concentrated in planar zones which impart a crude flow foliation to the rock (Fig. 3).

All samples are sparsely phyric with <1% phenocrysts of plagioclase and very rare clinopyroxene. Plagioclase is usually the sole phenocryst phase and occurs as euhedral, prismatic crystals that range in length from <0.1 to 1.5 mm. Plagioclase glomerocrysts are common, and many plagioclase crystals display weak compositional zonation (Fig. 4). In the glassy to microcrystalline samples, individual crystals have well-developed quench overgrowths suggesting rapid cooling of a fluid lava. One sample (142-864A-1M-6, 75–134 cm, Piece 1) contains a single, small (0.4 mm), euhedral crrystal of clinopyroxene.

The groundmass consists of varying proportions of glass, plagioclase, olivine, clinopyroxene, titanomagnetite, sulfide globules and dark, cryptocrystalline mesostasis. Groundmass textures vary from glassy to intergranular. Over this range of textures, plagioclase is the most abundant groundmass phase and may comprise up to 40% of the groundmass in coarser-grained samples. All crystals are acicular and skeletal, and range in size from <0.05 to 1.5 mm in length. These often occur in sheaf, bow-tie, or radial arrangements. Olivine (0 to 2 volume percent [vol%], <0.03 to 0.2 mm) occurs as acicular microlites and/or equant, skeletal crystals. The microlites are often in sheaf or bow-tie

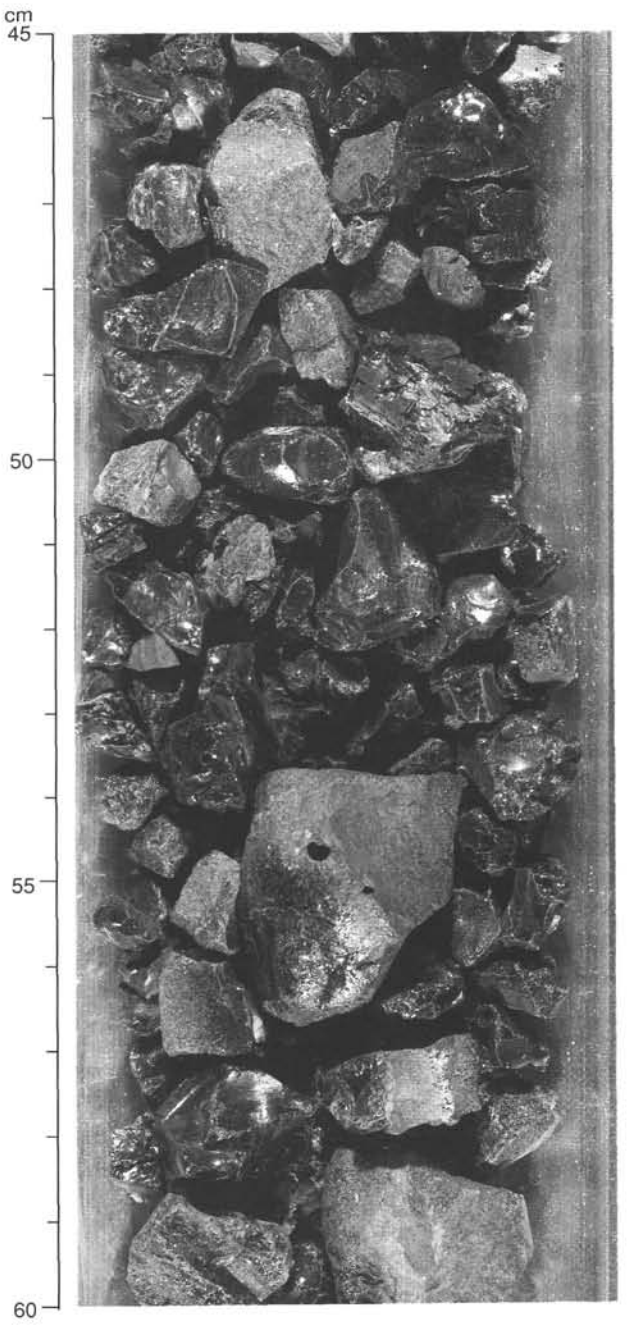

Figure 2. Representative glassy to fine-grained crystalline samples from interval 142-864A-1M-5, 45–60 cm. Some fragments have glassy chill margins grading into crystalline interiors. Note the rounding (due to drilling and milling) of many crystalline samples.

arrangements and commonly lie at the centers of individual spherules. Clinopyroxene (0 to 40 vol%, ≤0.3 mm), absent from glassy and spherulitic samples, occurs either as cryptocrystalline, plumose aggregates or as anhedral, granular, and sometimes skeletal crystals. The latter occur in samples with intergranular groundmasses where clinopyroxene is intergrown with plagioclase in a subophitic texture. Titanomagnetite (0 to 2 vol%) is present in samples with variolitic to intergranular groundmasses where it occurs as small (<0.005 to 0.01 mm), skeletal and/or cruciform-shaped crystals concentrated in

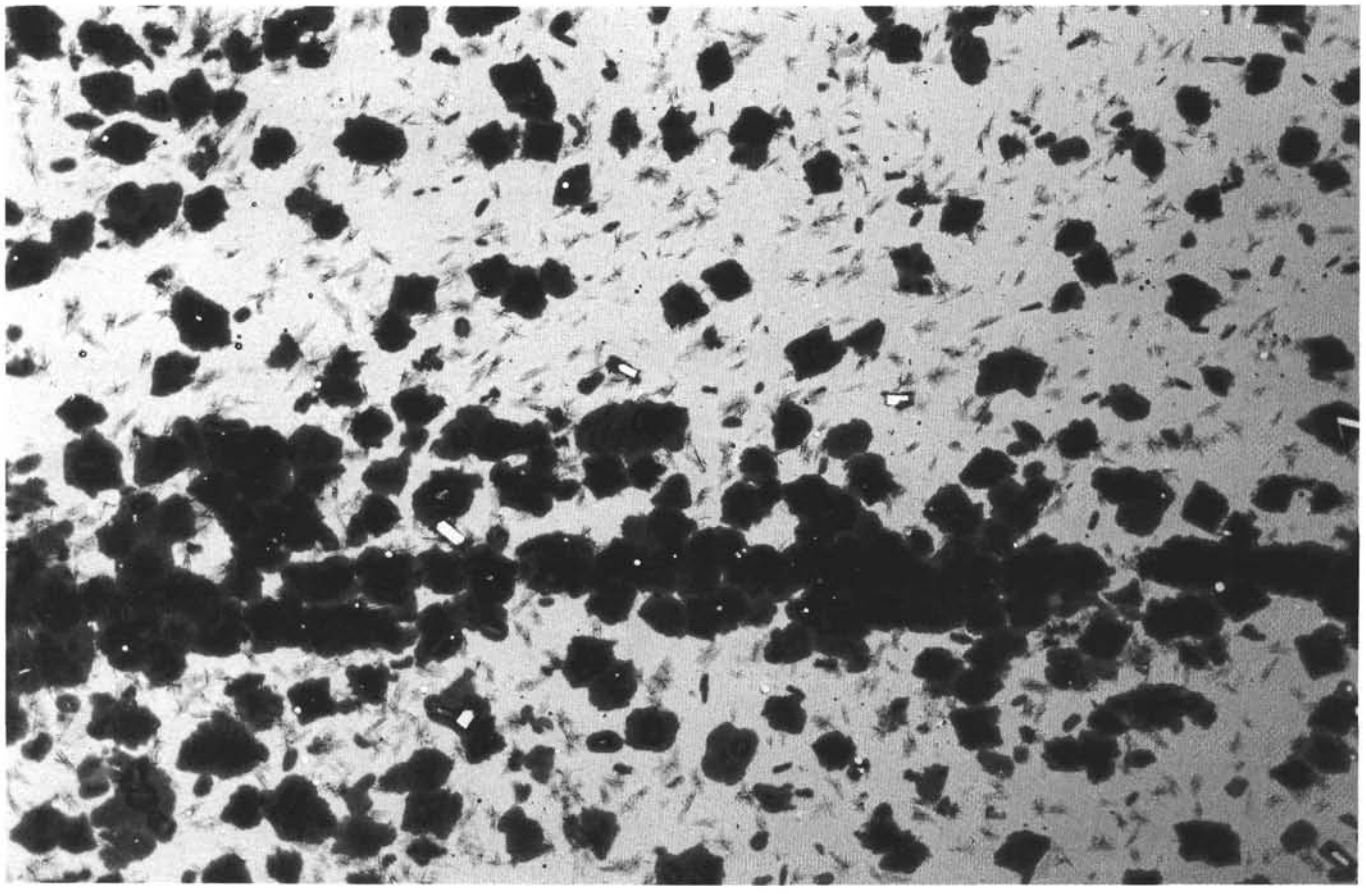

Figure 3. Photomicrograph (polarized light) of sample from interval 142-864A-IM-2, 0–35 cm, showing a crude flow foliation defined by a planar concentration of spherules. Photograph is 5.6 mm across.

the mesostasis between spherules or interconnected silicate minerals. Two varieties of primary sulfide globules are present in trace amounts. The first variety, present solely within glassy samples, consists of small (<8–10 μm) bright yellow, anisotropic (in polarized light) globules. By analogy to previous studies (Allan et al., 1989; Mathez, 1976; Czamanske and Moore, 1977), these likely represent immiscible liquids of pyrrhotite. The second variety, concentrated in the mesostasis of microcrystalline or fine-grained samples, occurs as very small (<5 μm), pale yellow, isotropic globules tentatively identified as pyrite (Fig. 5). Very small (<1–2 μm) sulfide globules also occur, rimming the walls of small vesicles.

The vesicle contents range from 0% to 6%, with coarser-grained samples displaying a higher percentage. Vesicles show a wide range in size, shape, and distribution wherein small (<0.05 mm) vesicles are round and evenly distributed and larger ones (0.1 to 2 mm) are irregular and concentrated in patchy and/or planar zones.

Traces of hydrothermal alteration are occasionally found as milky-white to yellowish-green amorphous silica(?) or reddish-brown Fe-oxyhydroxide material coating the outer surfaces of glassy and crystalline samples (Fig. 6) or the inner walls of small cavities. A few small grains (<0.1 mm) are probably quartz. Fine-grained, secondary sulfide minerals (Cu-rich?) and associated blue-green microcrystalline Cu-sulphate(?) minerals are sparsely present in some coarser-grained samples.

Unit 2: Aphyric to Slightly Plagioclase Phyric Basalt

Rock fragments assigned to Unit 2 were recovered from the lower portion of Hole 864A (Cores 142-864A-3Z, -4Z, and -5Z) and are distinguished from those of Unit 1 on the basis of geochemistry and degree of rock crystallinity. Fresh, nonglassy, angular to subrounded fragments range in size from 1 to 5 cm in diameter. All fragments are massive, microcrystalline to fine-grained crystalline, nonfoliated, and slightly vesicular. One sample (142-864A-4Z, 9–14 cm) displays a well-developed, polygonal outline and may be a portion of a radial or columnar joint (Fig. 7).

Samples are aphyric to sparsely phyric with up to 2 vol% phenocrysts of plagioclase and very rare olivine. Plagioclase is usually the sole phenocryst phase and occurs as euhedral, tabular to prismatic crystals that range from 0.03 to 2.1 mm in length. Glomerocrysts are common. A few phenocrysts are subhedral and show evidence of resorption. Most crystals display weak compositional zonation and well-developed quench overgrowths. One sample (142-864A-5Z-1, 0–5 cm) contains a single, small (0.25 mm) euhedral phenocryst of olivine.

The groundmass consists of varying proportions of plagioclase, olivine, clinopyroxene, titanomagnetite, sulfide globules, and dark, cryptocrystalline mesostasis. Quench-growth groundmass textures vary from variolitic and microlitic to intersertal or intergranular. Plagioclase crystals (2% to 40%, <0.02 to 1.5 mm) are acicular and skeletal and occur either individually or in sheaf, bow-tie, or radial aggregates. Olivine (1 to 4 vol%, <0.1 to 0.5 mm in length) occurs as acicular microlites in sheaf or bow-tie bundles or as equant, skeletal crystals. Clinopyroxene (0 to 40 vol%, ≤0.2 mm) occurs either as cryptocrystalline, plumose aggregates, or as anhedral, granular, and sometimes skeletal crystals. The latter is found in samples with intergranular groundmasses where clinopyroxene is intergrown with plagioclase in a subophitic texture. Titanomagnetite (1 to 5 vol%) is present in all samples and occurs as small (<0.005 to 0.01 mm), skeletal and/or

Figure 4. Photomicrograph (crossed polars) of Sample 142-864A-5Z-1, 15–19 cm, showing a plagioclase glomerocryst set within a microlitic groundmass of acicular plagioclase and granular clinopyroxene and olivine. This sample is actually from Unit 2 but is typical of glomerocrysts observed in both units. Note compositional zonation and well-developed quench overgrowths. The photograph is 3.7 mm across.

cruciform-shaped crystals concentrated in cryptocrystalline mesostasis. Trace amounts of very small (typically 1–2 μm), spherical, isotropic, pale-yellow sulfide globules (pyrite?) also occur in the mesostasis.

Two samples (142-864A-3Z-1, Piece 1, and 142-864A-4Z-1, Piece 3) contain large (up to 1 cm diameter) crystal clots of clinopyroxene and plagioclase (see Fig. 8). Large (up to 3 mm in length), elongated, euhedral crystals of poikilitic clinopyroxene are intergrown with similarly large (up to 2.5 mm in length), euhedral prismatic crystals of plagioclase. Under crossed polars, individual clinopyroxene crystals display a mosaic pattern of small, optically continuous regions (Fig. 8) which most likely reflect deformation during rapid crystal growth (e.g., Bryan, 1972). Plagioclase crystals are weakly zoned and sometimes skeletal. The euhedral crystal outlines, occasional skeletal textures, and growth deformation textures all suggest rapid crystallization from a liquid. Trace amounts of large (up to 0.01 mm), spherical to irregularly shaped sulfide grains (pyrite?) are interstitial to the plagioclase and clinopyroxene (Fig. 9). It is unclear whether these crystal clots are cognate or xenolithic.

The vesicle content of Unit 2 ranges from 0% to 5%. Vesicles are round to irregular in shape and range in size from 0.005 to 3 mm in diameter. Unlike Unit 1, which displayed localized concentrations of large vesicles, all vesicles in Unit 2 are evenly dispersed throughout all samples.

Traces of hydrothermal alteration are occasionally found as milky-white to yellowish-green amorphous silica(?) and/or reddish-brown Fe-oxyhydroxide material coating outer surfaces of the rock fragments. Rust-colored clay minerals(?) are occasionally found partially filling vesicles.

Geochemistry

Thirteen whole-rock and hand-picked glass samples from Unit 1 and two whole-rock samples from Unit 2 were selected for onboard geochemical analysis. Major and selected trace elements (V, Cr, Ni, Cu, Zn, Sr, Y, Zr, Nb, Ba, Ce, and Rb) were analyzed by X-ray fluorescence; however, data for Ba, Ce and Rb are below the detection limits. For further discussion of detection limits see Bach and Bostrom (this volume). All results are summarized in Table 2.

The data show that the rocks are typical depleted N-MORB (Fig. 10). Figure 11 shows TiO_2 variation diagrams for Fe_2O_3, Na_2O, Al_2O_3, and CaO. In Figure 12, Ti, Y, and Cr are plotted against Zr. Two important features should be noted. First, all analyzed samples from within either Unit 1 or Unit 2 yield very similar major and trace element values, considering the analytical precision. Second, Unit 1 and Unit 2 are geochemically distinct from each other. Together these results confirm the petrographic-based conclusion that the various junk-basket (Core 142-864A-1M), wash-core (Core 142-864B-2W), and DCS core (Cores 142-864A-3Z to -5Z) samples represent two distinct lithologic units. Based on both major and trace element abundances, Unit 2 appears to be more primitive than Unit 1, being characterized by slightly higher $Mg/(Mg + Fe^{2+})$, Al_2O_3, CaO, and Cr, and slightly lower TiO_2, Fe_2O_3, Na_2O, Zr, and Y (Table 2, Figs. 11 and 12).

CO_2 and H_2O abundances of rock powders from both Unit 1 and Unit 2 were measured by elemental organic analysis techniques on a Carlo-Erba CHNS machine. In general, fine-grained crystalline samples show slightly higher H_2O contents, perhaps due to alteration or addition during crystallization.

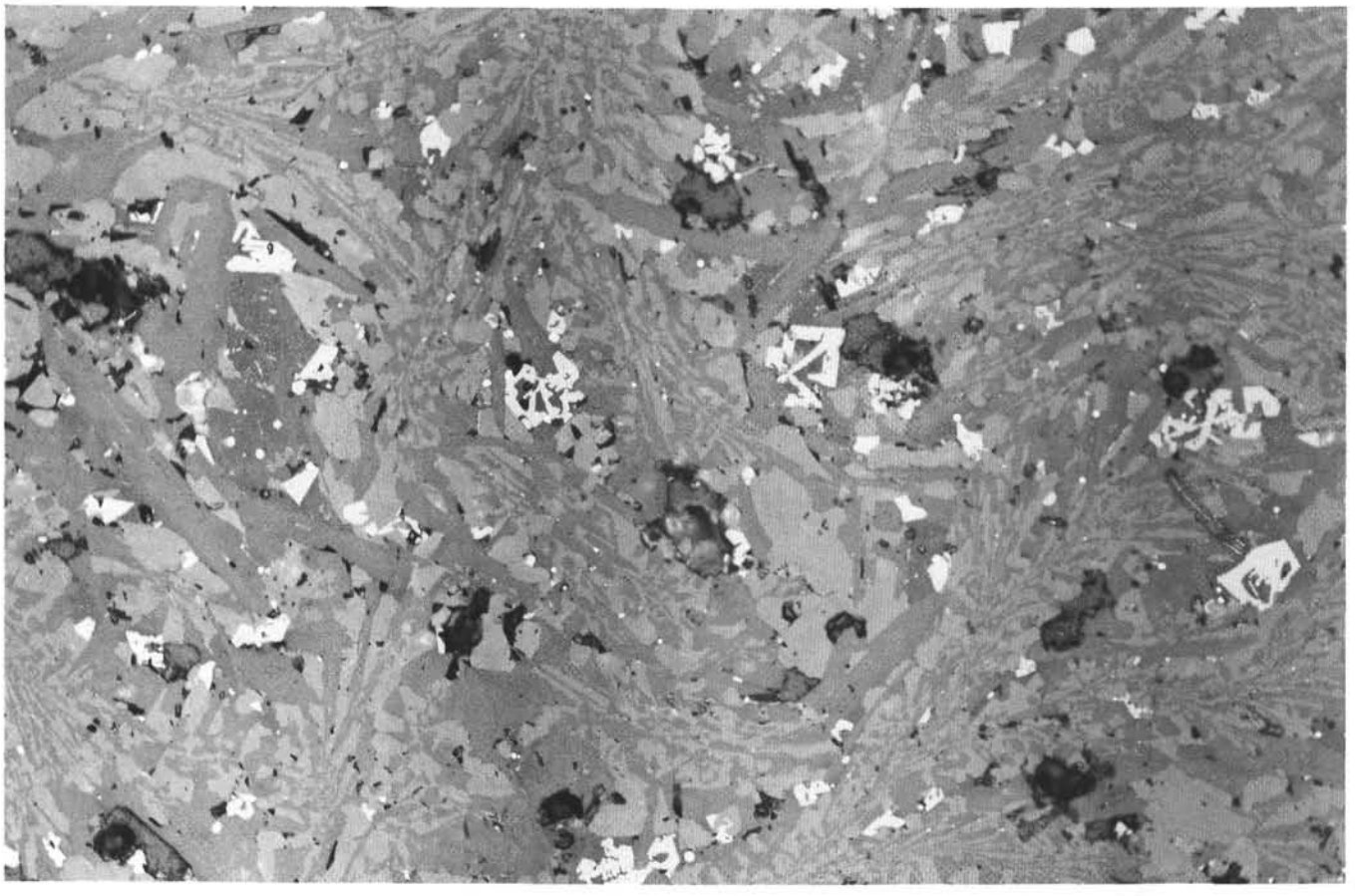

Figure 5. Photomicrograph (reflected light) of Sample 142-864A-4Z-1, Piece 3, showing small (1–2 µm) spherical globules of pyrite set within typical cryptocrystalline mesostasis. Also note the skeletal, cruciform-shaped titanomagnetite crystals dispersed throughout the sample. This sample is from Unit 2 but is typical of sulfide globule-bearing samples from both units. The photograph is 0.67 mm across.

Comparison of Units 1 and 2 with other "zero-age" dredged samples from the same area (Batiza and Niu, 1992) reveals a similar trend of compositional variability (Fig. 13). The dredge samples of Batiza and Niu (1992) vary in $Mg/(Mg + Fe^{2+})$ from 0.65 to 0.52. Site 864 samples fall on the same liquid-line-of-descent trends defined by the dredge samples, but toward the lower $Mg/(Mg + Fe^{2+})$ end (Fig. 13).

By analogy with detailed fractionation models of Batiza and Niu (1992), the limited data from Site 864 suggest that both Unit 1 and Unit 2 could be derived from more primitive (higher $Mg/[Mg + Fe^{2+}]$) lavas in the area through low-pressure fractional crystallization of plagioclase, olivine, and clinopyroxene. Furthermore, because the two Site 864 units fall within the general liquid line of descent defined by other lavas in the 9°30′N EPR region, it is possible that all of the observed N-MORB in this region could have been derived from compositionally similar parental magmas, silicate liquids which were deduced by Batiza and Niu (1992) to have been produced by ≈18% partial melting of a relatively depleted mantle source.

MAGNETISM

The principal objective of paleomagnetic studies on zero-age mid-oceanic rocks is to investigate the acquisition of initial magnetization of the rocks constituting the basaltic layer. Natural remanent magnetization and susceptibility measurements were made on the Leg 142 samples recovered from the uppermost 15.0 m of the oceanic floor to examine the variation in magnetic properties with lithology. In general, the results of these measurements indicate that both the NRM intensity and susceptibility of the samples are comparable to those of previously sampled basalts from the Mid-Atlantic Ridge (Hamano et al., 1980; Shipboard Scientific Party, 1988; Prevot et al., 1979). As all the samples recovered are unoriented and their relative positions as to depth are uncertain, it was not possible to study the variation of the NRM inclination or its alteration with depth.

Natural Remanent Magnetization and Coercivity

The intensity of NRM of the samples varies from 0.17 A/m to 49 A/m (Table 3). The lowest value is found in a glass-rich sample probably from a lobated flow, whereas fairly high values are obtained for samples from interiors of more massive flows. Table 4 shows a comparison of the NRM intensities of the samples from Leg 142 with those obtained for Mid-Atlantic Ridge basalts sampled by DSDP Leg 52, ODP Leg 106, and by the FAMOUS submersible dives (Hamano et al., 1980; Shipboard Scientific Party, 1988; Prevot et al., 1979).

The behavior of the samples during alternating field (AF) demagnetization, or magnetic cleaning, indicates that the NRM of these samples is of low stability. Values of the median destructive field (MDF), the field required to remove one half of the initial NRM (J_0), were determined from the AF demagnetization curves for the samples and are listed in Table 4. The MDF values (with a mean of 12.6 mT) are substantially lower than those of the oceanic basalts samples from the Mid-Atlantic Ridge, which have a mean MDF of 69 mT with a standard deviation of 29 mT (Shipboard Scientific Party, 1988). Typical demagnetization curves for the NRM are shown in Figure 14. In general the NRM of the samples, after studying their Zijderveld

Table 2. Geochemical analyses of major and selected trace elements, Site 864.

Hole:	864A	864A	864A	864A	864A	864A	864A	864A	864A
Core, section:	1M-1	1M-2	1M-2	1M-3	1M-3	1M-3	1M-3	1M-4	1M-5
Interval (cm):	0–10	0–35	0–35	0–35	0–35	55–85	100–150	0–9	0–100
Comments:	WR	Glass	Glass	Coarse glass	Medium glass	WR	WR	WR	Glass
Unit:	1	1	1	1	1	1	1	1	1
SiO_2	49.75	49.69	49.94	49.80	50.09	50.00	49.96	50.00	49.82
TiO_2	1.62	1.63	1.64	1.64	1.64	1.64	1.66	1.65	1.63
Al_2O_3	14.50	14.22	14.27	14.28	14.38	14.27	14.27	14.35	14.27
Fe_2O_3	11.50	11.61	11.58	11.60	11.63	11.65	11.68	11.68	11.66
MnO	0.22	0.20	0.20	0.20	0.20	0.20	0.20	0.21	0.20
MgO	7.16	7.26	7.40	7.21	7.52	7.33	7.35	7.20	7.40
CaO	11.73	11.68	11.65	11.68	11.75	11.75	11.70	11.80	11.67
Na_2O	2.54	2.52	2.59	2.59	2.56	2.51	2.53	2.49	2.59
K_2O	0.13	0.13	0.13	0.13	0.13	0.16	0.13	0.21	0.13
P_2O_5	0.09	0.10	0.11	0.10	0.10	0.11	0.10	0.10	0.12
Total	99.23	99.03	99.51	99.22	100.00	99.61	99.58	99.70	99.49
LOI	–0.47	–0.60	–0.71	–0.75	–0.33	–0.61	–0.69	0.08	–0.83
CO_2	0.07	0.01	0.01	0.02	0.02	0.05	0.04	0.05	0.03
H_2O	0.39	0.18	0.15	0.16	0.16	0.32	0.24	0.48	0.13
Mg#	0.578	0.579	0.584	0.577	0.587	0.580	0.580	0.576	0.583
V	346	361	357	359	358	346	355	337	361
Cr	241	240	236	239	242	234	235	225	240
Ni	73	74	73	72	79	73	74	66	76
Cu	76	74	79	74	114	73	75	72	75
Zn	89	92	96	94	108	88	91	83	93
Sr	118	121	121	122	122	123	122	123	122
Y	35.4	35.9	36.3	36.9	36.5	35.6	36.7	35.9	36.7
Zr	109	111	113	112	111	111	112	109	111
Nb	2.8	3.1	2.8	3.2	3.1	3.0	2.5	3.0	2.6
Zr/Y	3.08	3.09	3.11	3.02	3.05	3.12	3.06	3.04	3.04
Nb/Zr	0.026	0.028	0.025	0.029	0.028	0.027	0.022	0.027	0.023
Ti/Zr	89.2	88.3	87.1	88.0	88.3	88.3	88.4	90.3	87.8
Or	0.77	0.77	0.8	0.79	0.94	0.8	0.8	1.27	0.8
Ab	21.72	21.55	22.18	22.16	21.5	21.93	21.65	21.33	22.21
An	28.12	27.44	27.23	27.27	27.53	27.66	27.52	27.66	27.22
Di	24.72	25.06	25.04	25.18	25.2	25.12	25.06	25.37	25.08
Hy	16.42	16.86	16.11	15.98	17.16	16.04	17.14	16.71	15.42
Ol	2.58	2.39	3.17	2.88	2.29	3.46	2.41	2.36	3.75
Mt	1.69	1.7	1.7	1.7	1.71	1.71	1.71	1.71	1.71
Il	3.11	3.14	3.15	3.15	3.14	3.15	3.18	3.16	3.13
Ap	0.21	0.22	0.24	0.22	0.24	0.23	0.22	0.23	0.27

Notes: Rb, Bu, and Ce abundances are below 1, 15, and 20 ppm, respectively, for all samples. Mg# refers to $Mg/(Mg + Fe^{2+})$ where Fe^{2+} is assumed to be 0.9 times Fe_{total}; LOI refers to loss on ignition. BAS142 is a hand-picked glass composite used as an in-house standard (see "Explanatory Notes" chapter, this volume). WR = whole-rock sample.

plots, could be interpreted to consist of two components: a relatively stable component (primary magnetization of thermoremanent origin) and an unstable component of secondary magnetization acquired probably during the recovery of drilled core and/or during the laboratory operations of drilling and sawing of minicores. The Zijderveld plots clearly indicate the secondary magnetization to be of very low magnetic coercivity, typically <10 mT (Fig. 15).

To study the NRM-ARM (anhysteretic remanent magnetization) relationship, ARM was given to the samples in the laboratory after completion of the AF demagnetization studies. For most samples the demagnetization curves for the ARM were, as expected, found to be similar in shape to those of NRM demagnetization curves. Typical parallelism between the ARM and NRM behavior is shown in Figure 16. The median destructive field values (at which $J/J_0 = 0.5$) are remarkably similar in both cases, which indicates that the behavior of the ARM (which is known to have magnetic characteristics that are similar to that of thermoremanent magnetization, TRM) reflects the thermoremanent origin of the NRM.

Magnetic Susceptibility and the Q Ratio

Magnetic susceptibility (χ) is a measure of the instantaneous magnetization induced in a sample in the presence of an external field and it is an intrinsic property of composition, concentration, and grain size of the magnetic minerals within a rock. Values of χ determined for the Leg 142 samples are listed in Table 3. Compared with the variations in the NRM, the range in variation of susceptibility is large, the variation being of about two orders of magnitude over a span of 10 samples. A majority of samples (6 out of 10) have χ values in the intermediate range of $1–3 \times 10^{-2}$ SI. These values are typical for primary titanomagnetite grains with very low degrees of hydrothermal alteration. The lowest value obtained is that for the glass-rich Sample 142-864A-1M-3, 0–35 cm, from a rapidly quenched lobated flow or thin sheet.

The Koenigsberger ratio (Q) is a measure of the ratio of NRM and the magnetization induced in the rock by the present Earth's field (0.037 mT at Site 864). The Q values determined for the samples are listed in Table 3, and these are among the highest reported so far from oceanic ridge basalts. The mean Q value for the Leg 142 samples is 56.4 (with a standard deviation of 39.8), indicating that the uppermost part of the basaltic layer is very strongly dominated by the remanent component of magnetization and the induced component is of insignificant proportion.

Rock Magnetic Parameters and Magnetic Mineralogy

The relatively meager recovery of core material during Leg 142 gave sufficient time to complete a few additional magnetic investiga-

Table 2 (continued).

864A 1M-5 0–100 BAS142 1	864A 1M-6 0–75 Glass 1	864A 1M-6 75–135 WR 1	864B 2W-1 16–18 WR 1	Unit 1 Average	Unit 1 1σ	864A 4Z-1 Piece 2 WR 2	864A 5Z-1 Piece 7 WR 2	Unit 2 Average	Unit 2 1σ
49.98	49.90	50.04	49.90	49.91	0.12	49.78	49.64	49.71	0.10
1.64	1.64	1.64	1.65	1.64	0.01	1.75	1.80	1.78	0.04
14.28	14.27	14.31	14.19	14.30	0.08	14.10	13.97	14.03	0.09
11.59	11.63	11.60	11.57	11.61	0.05	11.96	12.22	12.09	0.18
0.20	0.20	0.20	0.20	0.20	0.01	0.21	0.21	0.21	0.00
7.40	7.34	7.21	7.20	7.30	0.11	7.27	7.02	7.15	0.18
11.70	11.69	11.77	11.76	11.72	0.05	11.50	11.41	11.45	0.06
2.55	2.58	2.58	2.57	2.55	0.03	2.65	2.62	2.63	0.02
0.13	0.13	0.14	0.17	0.14	0.02	0.15	0.14	0.14	0.00
0.10	0.13	0.10	0.12	0.11	0.01	0.11	0.12	0.12	0.01
99.56	99.51	99.59	99.33	99.49		99.46	99.14	99.30	
–0.58	–0.83	–0.41	–0.16			–0.76	–0.88		
0.03	0.04	0.02	0.04			0.07	0.02		
0.17	0.23	0.45	0.26			0.28	0.20		
0.584	0.581	0.577	0.578	0.581	0.003	0.572	0.558	0.565	0.010
362	366	347	342	353	9	371	366	369	3
244	239	234	226	237	6	201	176	188	18
74	74	72	66	73	4	73	65	69	5
74	76	73	73	77	11	71	70	70	1
93	93	88	86	92	6	92	95	93	2
121	123	121	124	122	1	120	118	119	2
36.1	37.4	36.7	36.6	36.4	0.6	39.5	41.1	40.3	1.1
111	112	110	113	111	1	121	123	122	2
3.0	3.2	3.0	2.9	2.9	0.2	3.1	2.3	2.7	0.6
3.09	2.98	3.01	3.08	3.06	0.04	3.05	2.99	3.02	0.04
0.027	0.029	0.027	0.026	0.026	0.002	0.026	0.019	0.022	0.005
88.1	88.3	89.1	87.5	88.3	0.8	87.0	87.8	87.4	0.6
0.78	0.8	0.85	0.83	0.85	0.13	1.02	0.87	0.95	0.11
21.84	22.12	22.11	22.44	21.90	0.33	22.01	22.68	22.35	0.47
27.45	27.26	27.34	26.27	27.38	0.41	26.98	26.47	26.73	0.36
25.11	25.08	25.47	24.85	25.10	0.19	25.67	25.07	25.37	0.42
16.7	16.12	16.27	16.85	16.44	0.51	15.93	15.42	15.68	0.36
2.72	3.1	2.57	2.48	2.78	0.46	2.69	3.71	3.20	0.72
1.7	1.71	1.7	1.79	1.71	0.02	1.7	1.76	1.73	0.04
3.15	3.16	3.15	3.46	3.17	0.09	3.17	3.36	3.27	0.13
0.22	0.28	0.23	0.27	0.24	0.02	0.26	0.24	0.25	0.01

tions which are not part of standard procedure on ODP legs. Thermal demagnetization experiments and saturation isothermal remanent magnetization (SIRM) studies were made on a few representative samples to study the blocking temperature and saturation magnetization characteristics of the magnetic minerals and phases that are the dominant carriers of the remanent magnetization. Two samples were investigated for thermal behavior of the remanence which could provide diagnostic information about the composition of the minerals carrying the remanence. The decay of remanent intensity with temperature (J_t/J_0) shows low blocking temperatures (Fig. 17) in the range of 200°–300°C which are typical for titanium-rich titanomagnetites. The susceptibility of the samples was measured before every step of heating to check any chemical alterations (e.g., caused by oxidation) suffered by the magnetic minerals during the thermal treatment. The changes in susceptibility were observed to start at around 200°C and in one case (Fig. 18) a substantial reduction in susceptibility was observed between 300° and 600°C. This suggests that the titanomagnetite grains carrying the thermoremanence are of low thermal stability and therefore are more susceptible to alteration to titanohematite phase by oxidation. A thin section of this sample (142-864A-1M-4, 0–9 cm) made after completion of thermal studies, when examined for opaque minerals by a microscope, indicated reddish wisps in the mesostasis, suggesting the presence of the hematite phase.

The study of the saturation IRM on two coarser samples taken from massive flows indicated them to be magnetically very soft; the back field (B_{cr}) required for removing the SIRM was very low (<10 mT). The low coercivity of IRM is diagnostic for multidomain size (MD) titanomagnetite grains with $\chi = 0.6$ (Thompson and Oldfield, 1986). This suggests that MD titanomagnetites of grain size (of the order of some tens of microns) are the dominant carriers of the remanent magnetization in these samples.

The variation of low-field susceptibility from room temperature (298 K) to liquid nitrogen temperature (78 K) can provide information about the composition and grain-size distribution of titanomagnetites in basalts (Senanayke and McElhinny, 1981; Radhakrishnamurty, 1985; Sherwood, 1988). It is generally agreed that low values for the relative susceptibility ratio (K78/K298) in the range 0.1–0.5 (group 1) are indicative of Ti-rich titanomagnetites ($\chi = 0.5$–0.7), whereas ratios between 0.6 and 1.5 (group 2) can indicate single-domain (SD), Ti-poor magnetite grains. According to the low-temperature susceptibility behavior, 6 out of 10 samples studied belong to group 1 and the rest in group 2. One interpretation of these results is that both Ti-rich titanomagnetite MD grains and Ti-poor SD magnetite grains in varying proportion may be present in samples from Leg 142, the former being more dominant in six samples belonging to group 1. Detailed investigations of the opaque minerals may help to provide additional information about the composition of the iron-oxide minerals and their grain-size distribution.

PHYSICAL PROPERTIES

Index properties and compressional wave velocities, in both dry and saturated states, were measured on the samples recovered during Leg 142. All samples were unoriented and of relatively uncertain stratigraphic position due to extremely poor hole conditions. Due to

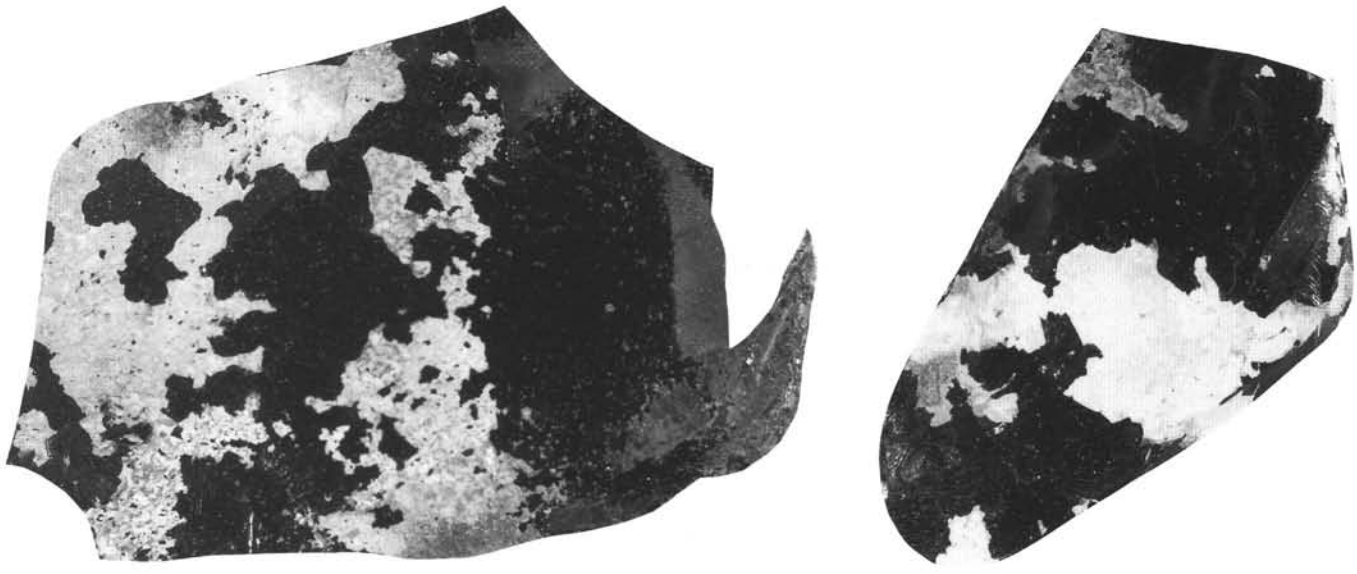

Figure 6. Hydrothermal alteration products coating fracture surfaces of glassy samples from Section 142-864A-1M-6.

Table 3. Rock magnetic parameters of Leg 142 samples.

Core, section, interval (cm), or piece number	NRM (A/m)	MDF (mT)	Susceptibility ($\times 10^{-2}$ SI)	Q	Susceptibility ratio (K78/K298)
142-864A-					
1M-3, 0–35	0.17	18	0.066	9	1.65
1M-4, 0–9	15.86	10	3.314	16	0.20
1M-4, 9–20	14.85	10	2.71	19	0.23
1M-5, 0–100	8.88	16	0.298	101	0.80
1M-5, 0–100	3.19	12	0.255	43	0.77
1M-6, 0–75	7.94	11	0.333	82	0.60
1M-6, 75–150	12.34	20	1.565	27	0.34
5Z-1, Piece 7	39.40	12	1.192	112	0.25
142-864B-					
2W-1, Piece 3	49.08	8	1.621	103	0.43
2W-1, Piece 3	28.55	9	1.854	52	0.39

Notes: NRM = natural remanent magnetization; MDF = median destructive field; Q = Koenigsberger ratio; and K78/K298 = susceptibility ratio at liquid nitrogen temperature to room temperature.

inadequate sample size, thermal conductivities of samples could not be obtained.

Index Properties

A total of seven samples were measured for index properties during Leg 142, including four minicores and three irregularly shaped samples. Only dry properties of the irregularly shaped samples were measured. To calculate the bulk and grain densities, porosities, and water contents of the minicores, wet and dry weights and dry volumes of the minicores were used. The Penta-pycnometer was found to provide erratic values of saturated sample volume, possibly due to diffusion of helium into pore water. Therefore, to calculate the saturated volumes of the minicores, the difference between the wet and dry weights of the samples were found, giving the weight and hence the volume of the seawater within the pore space, since the density of seawater is known. This volume was then added to the dry volume of the sample to approximate the bulk sample volume. Grain densities of the samples range from 2.84 to 3.02, while porosities range from 1.8% to 2.1%. Index properties of all samples are listed in Table 5.

Compressional Wave Velocities

Compressional wave velocities of four minicores were measured under dry and saturated conditions and at room pressure using the Hamilton frame velocimeter. The traveltime of a 500-kHz pulse through the sample was measured using a Nicolet 320 oscilloscope, and the lengths of the samples were measured using a digital caliper. All minicores were unoriented. Calculated compressional wave velocities (V_p) are listed in Table 6. Of interest are the relatively low V_p exhibited by three of the samples, all from lithologic Unit 1, under dry conditions. Porosity, including pore distribution and shape, have a strong influence on velocity (O'Connell and Budiansky, 1974; Toksöz et al., 1976; Wilkens et al., 1991). Low unsaturated velocities in these samples can be attributed to the influence of microcracks, or low-aspect-ratio pores, which would be open at atmospheric pressures (Toksöz et al., 1976). Sample 142-864A-5Z-1, Piece 7, from lithologic Unit 2, has the highest unsaturated velocity and displays little increase in velocity with saturation. Therefore, it is likely that high-aspect-ratio pores dominate in this specimen. In fact, this sample is known to have ≈6% by volume of spherical, closed vesicles (see "Igneous Petrology" section, this chapter).

REFERENCES*

Allan, J.F., Batiza, R., Perfit, M.R., Fornari, D.J., and Sack, R.O., 1989. Petrology of lavas from the Lamont Seamount Chain and Adjacent East Pacific Rise, 10° N. *J. Petrol.*, 30:1245–1298.

Batiza, R., and Niu, Y., 1992. Petrology and magma chamber processes at the East Pacific Rise ≈9°30′N. *J. Geophys. Res.*, 97:6779–6798.

Bryan, W.B., 1972. Morphology of quench crystals in submarine basalts. *J. Geophys. Res.*, 77:5812–5819.

Czamanske, G.K., and Moore, J.G., 1977. Composition and phase chemistry of sulfide globules in basalt from the Mid-Atlantic Ridge rift valley near 3° N. Lat. *Geol. Soc. Am. Bull.*, 88:587–599.

Hamano, Y., Nishitani, T., and Kono, M., 1980. Magnetic properties of basalt samples from DSDP Holes 417D and 418A. *In* Donnelly, T., Francheteau, J., et al., *Init. Repts. DSDP,* 51, 52, 53 (Pt. 2): Washington (U.S. Govt. Printing Office), 1391–1405.

* Abbreviations for names of organizations and publication titles in ODP reference lists follow the style given in *Chemical Abstracts Service Source Index* (published by American Chemical Society).

Mathez, E.A., 1976. Sulfur solubility and magmatic sulfides in submarine basalt glass. *J. Geophys. Res.*, 81:4269–4276.
O'Connell, R.J., and Budiansky, B., 1974. Seismic velocities in dry and saturated cracked solids, *J. Geophys. Res.*, 79:5412–5426.
Prevot, M., Lecaile, A., and Hekinian, R., 1979. Magnetism of the Mid-Atlantic Ridge crest near 37°N from FAMOUS and DSDP results: a review. *In Deep Drilling Results in the Atlantic Ocean: Oceanic Crust.* Am. Geophys. Union, Maurice Ewing Ser., 2:210–229.
Radhakrishnamurty, C., 1985. Identification of titanomagnetites by simple magnetic techniques and application to basalt studies. *J. Geol. Soc. India*, 26:640–651.
Senanayke, W.E., and McElhinny, M.W., 1981. Hysteresis and susceptibility characteristics of magnetite and titanomagnetites: interpretation of results from basaltic rocks. *Phys. Earth Planet. Inter.*, 26:47–55.
Sherwood, G.J., 1988. Rock magnetic studies of Miocene volcanics from Eastern Otago and Banks Peninsula, New Zealand: comparison between Curie temperature and low temperature susceptibility behaviour. *N.Z. J. Geol. Geophys.*, 31:225–235.
Shipboard Scientific Party, 1988. Site 648. *In* Detrick R., Honnorez, J., Bryan, W.B., Juteau, T., et al., *Init. Repts. DSDP,* 106/109 (Pt. A): Washington (U.S. Govt. Printing Office), 68–76.
Sun, S.S., and McDonough, W.F., 1989. Chemical and isotopic systematics of oceanic basalts: implications for mantle processes. *In* Saunders, A.D., and Norry, M.J. (Eds.), *Magmatism in the Ocean Basins.* Geol. Soc. Spec. Publ. London, 42:313–345.
Thompson, R., and Oldfield, F., 1986. *Environmental Magnetism:* London (Allan and Unwin).
Toksöz, N., Cheng, C.H., and Timur, A., 1976. Velocities of seismic waves in porous rocks. *Geophysics,* 41:621–645.
Weaver, J.S., and Langmuir, C.H., 1990. Calculation of phase equilibrium in mineral-melt systems. *Comput. Geosci.,* 16:1–19.

Ms 142IR-104

NOTE: For all sites drilled, core-description forms ("barrel sheets") and core photographs have been reproduced on coated paper and can be found in Section 4, beginning on page 75. Thin-section data are given in Section 5, beginning on page 89.

Table 4. Comparison of NRM and susceptibilities in Leg 142 samples and Mid-Atlantic Ridge basalts.

Leg	NRM (A/m)	Standard deviation	Susceptibility ($\times 10^{-2}$ SI)	Standard deviation
[a]Leg 106	11.0	4.2	1.27	0.56
[b]FAMOUS	14.4	12.3	0.30	0.03
[c]Leg 52	11.9	7.3	2.00	0.85
[d]Leg 142	18.0	16.0	1.46	1.08

[a]Peterson and Wooldridge (1988)
[b]Prevot et al. (1979)
[c]Hamano et al. (1980)
[d]This study

Table 5. Index properties of samples from Site 864.

Core, section, interval (cm), or piece number	Depth (mbsf)	Wet-bulk density (g/cm^3)	Grain density (g/cm^3)	Wet porosity (%)	Dry porosity (%)	Water content (%)
142-864A-						
1M-3, 0–35	0–6.6		2.85			
1M-4, 0–9	0–6.6	2.94	3.01	1.90	2.00	0.70
1M-5, 0–100	0–6.6		3.01			
1M-5, 0–100	0–6.6		2.84			
5Z-1, Piece 7	13.5–15.0	2.95	2.99	2.10	2.20	0.70
142-864B-						
2W-1, Piece 3	0–3.0	2.99	3.02	1.80	1.80	0.60
2W-1, Piece 3	0–3.0	2.98	3.01	1.80	1.80	0.60

Table 6. Compressional wave velocities of samples under dry and saturated conditions.

Core, section, interval (cm), or piece number	Depth (mbsf)	Wet velocity (m/s)	Dry velocity (m/s)
142-864A-			
1M-4, 0–9	0–6.6	4780	3071
5Z-1, Piece 7	13.5–15.0	5128	4923
142-864B-			
2W-1, Piece 2	0–3.0	4127	2924
2W-1, Piece 3	0–3.0	4364	3114

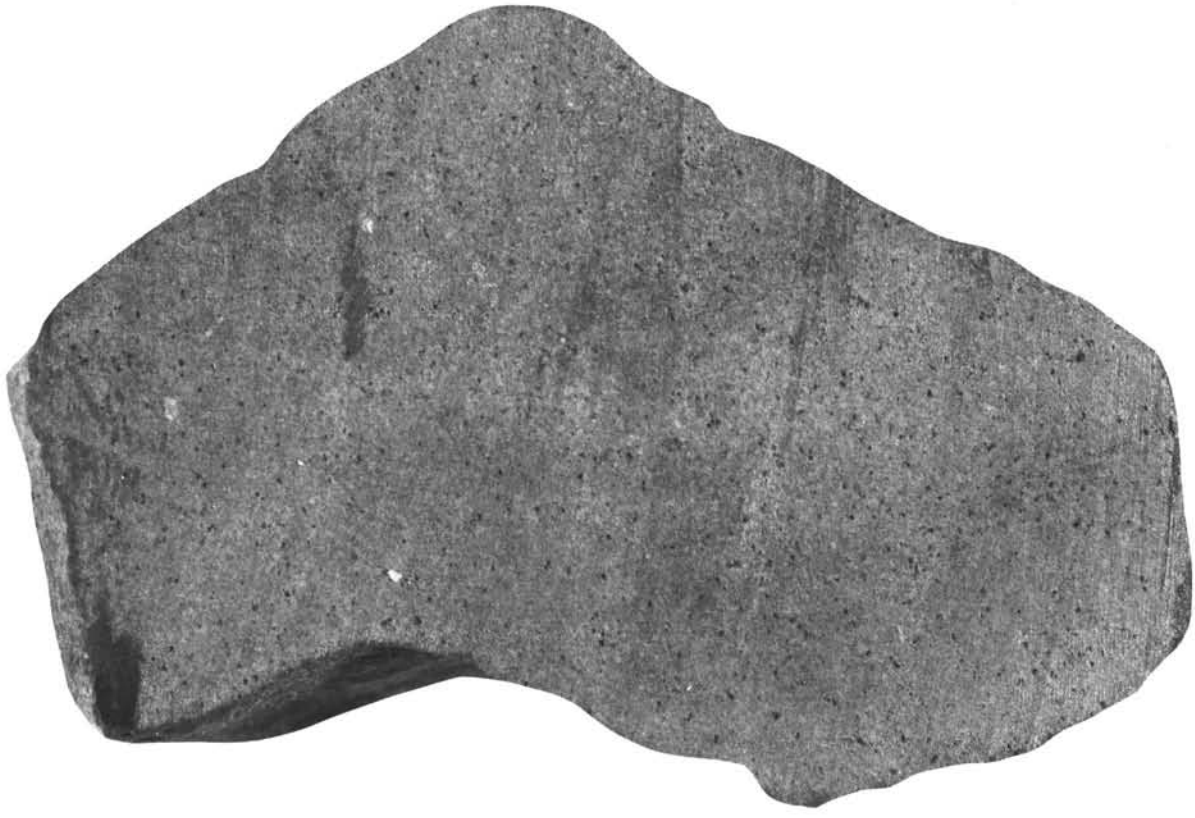

Figure 7. Photograph of Sample 142-864A-4Z-01, 9–14 cm, in plan view, showing the well-developed polygonal (hexagonal) jointing believed to represent columnar or radial jointing during cooling.

Figure 8. Photomicrograph (crossed polars) of Sample 142-864A-4Z-1, Piece 3, showing a large crystal clot of intergrown poikilitic clinopyroxene and plagioclase. Note the mosaic of optically continuous regions within individual clinopyroxene crystals. The photograph is 5.6 mm across.

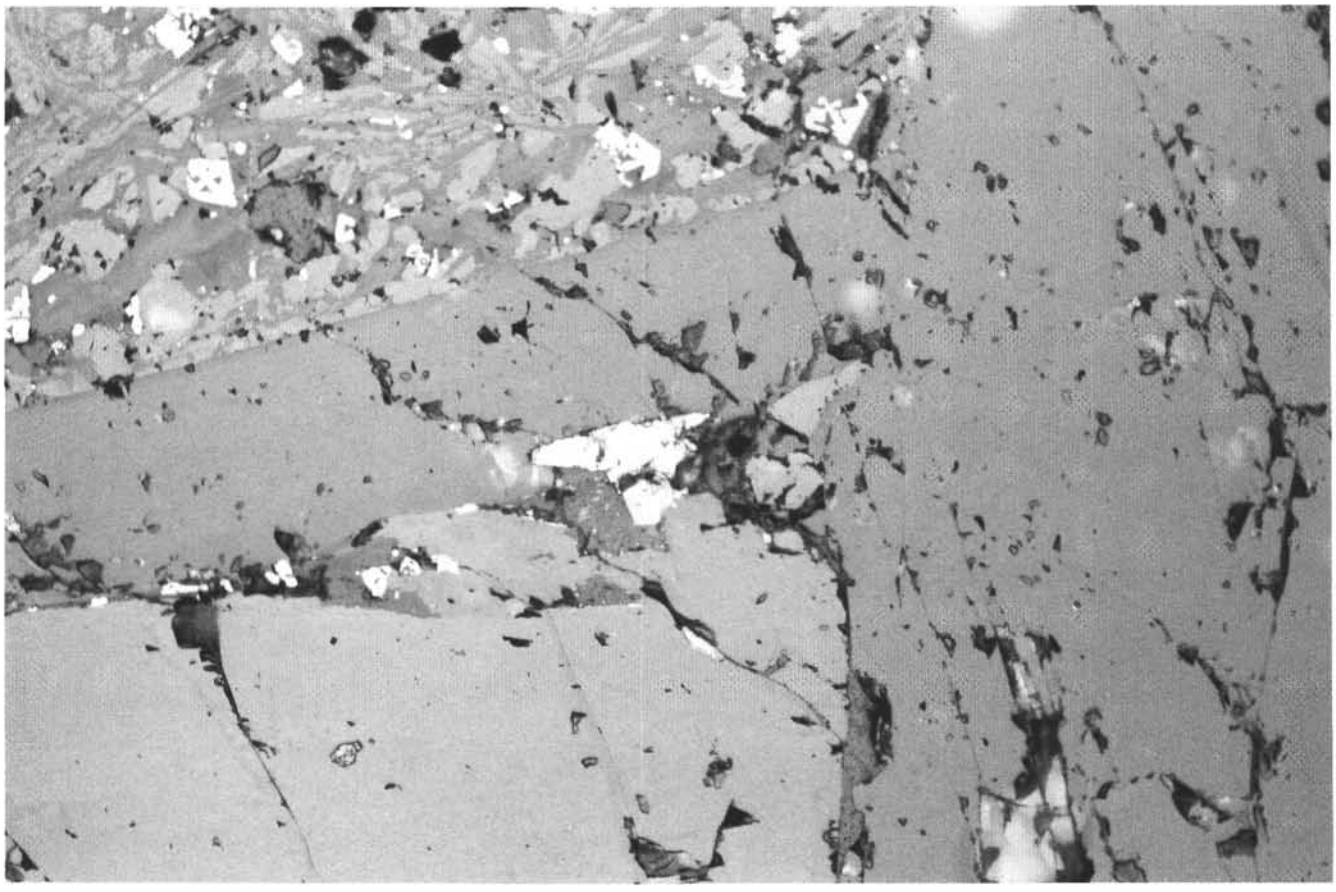

Figure 9. Photomicrograph (reflected light) of a portion of the crystal clot shown in Figure 8 showing a single, irregular grain of pyrite. The photograph is 0.67 mm across.

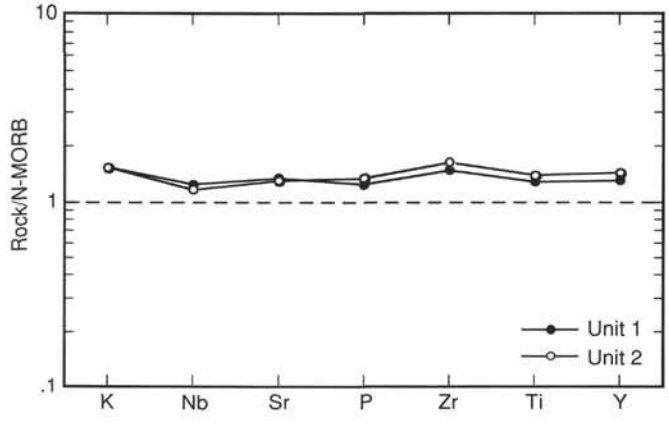

Figure 10. Average compositions of Units 1 and 2 normalized to standard N-MORB composition (Sun and McDonough, 1989). Leg 142 units are typical N-MORB in composition.

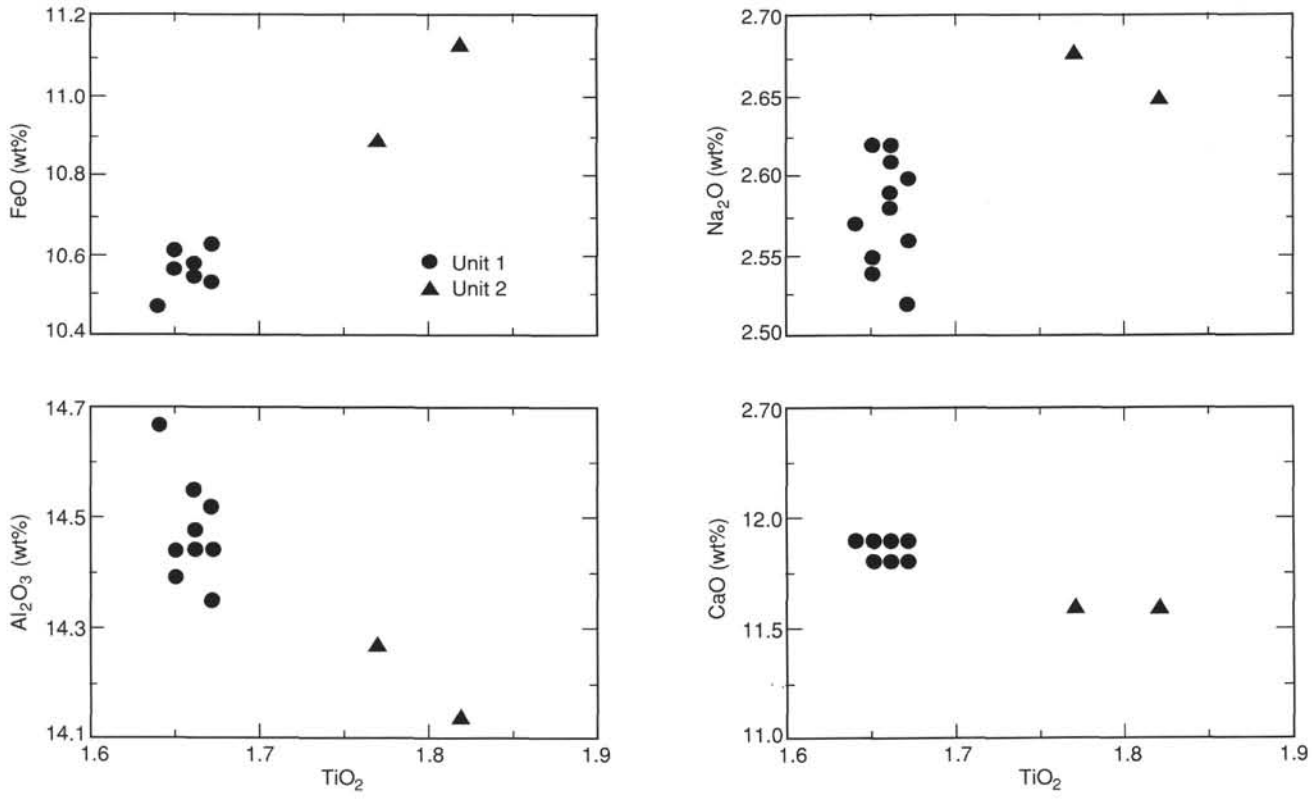

Figure 11. TiO_2 vs. Al_2O_3, FeO, Na_2O, and CaO variation diagrams for all analyzed samples from Site 864. The analytical results show that Unit 1 is distinct from Unit 2.

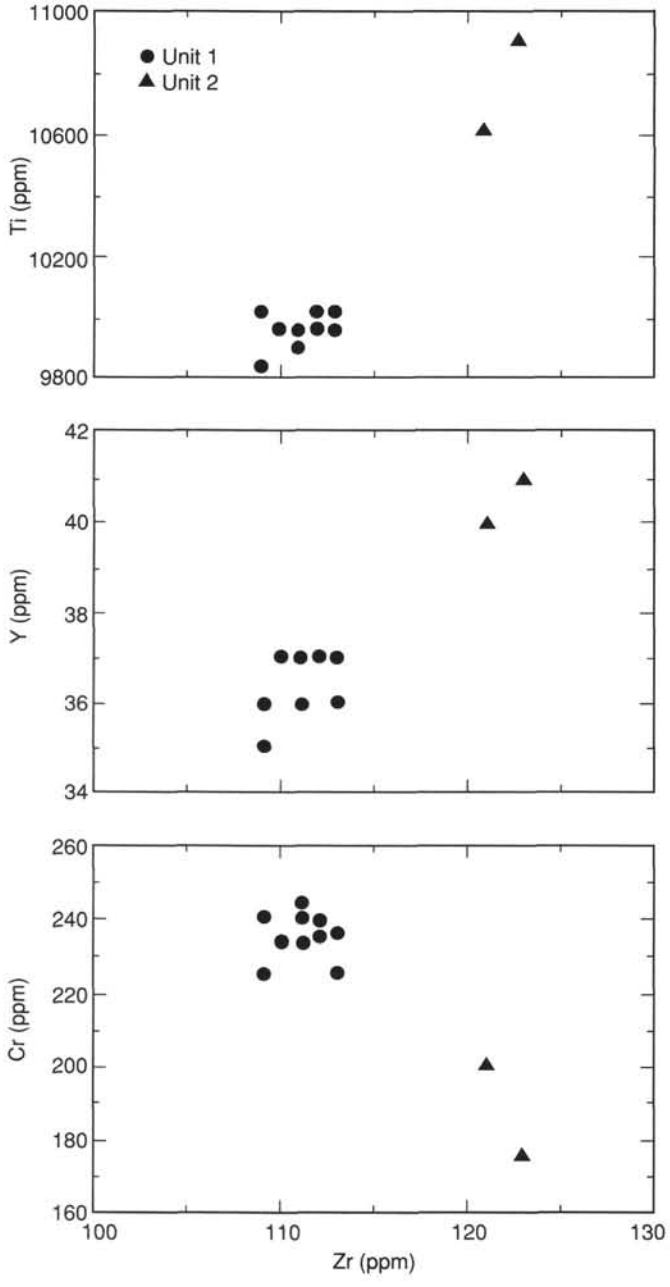

Figure 12. Zr vs. Ti, Y, and Cr variation diagrams for all analyzed samples from Site 864. Unit 2 has higher concentrations of incompatible elements (e.g., Zr, Ti, and Y), and lower concentration of compatible elements (e.g., Cr) than Unit 1.

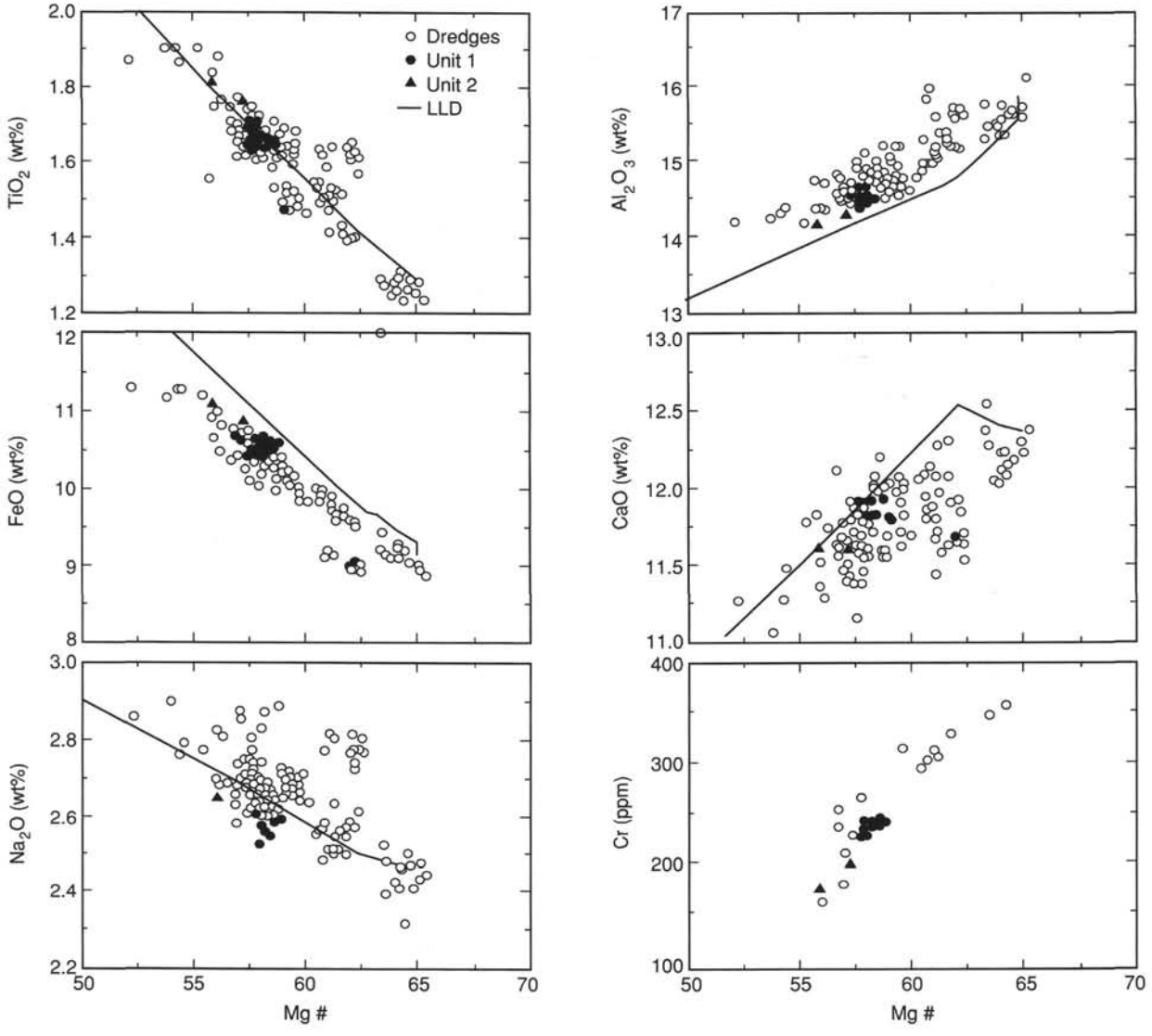

Figure 13. Geochemical comparison of all analyzed samples from Site 864 with dredged samples from the same area of the EPR at 9°30′N (Batiza and Niu, 1992). These diagrams show that Unit 1 and Unit 2 fall within the trend of compositional variability of the dredged samples, but fall in the lower $Mg/(Mg + Fe^{2+})$ end of the spectrum. The solid lines show calculated low-pressure liquid lines of descent (LLD), using the model of Weaver and Langmuir (1990).

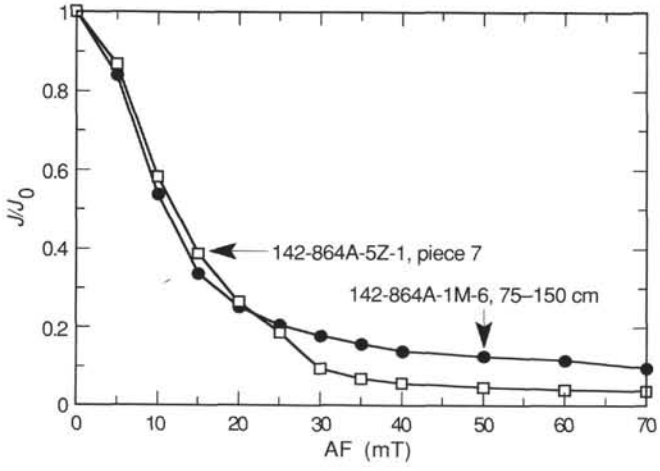

Figure 14. Typical alternating field demagnetization curves for the NRM of samples.

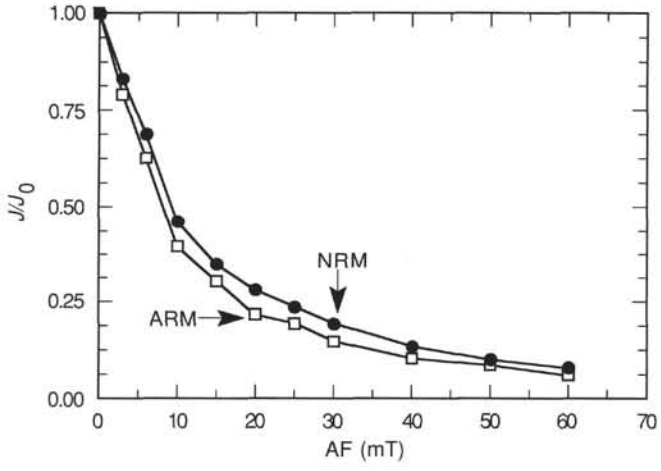

Figure 16. ARM-NRM relationship for Sample 142-864A-1M-4, 9–20 cm, during the alternating field demagnetization of a sample.

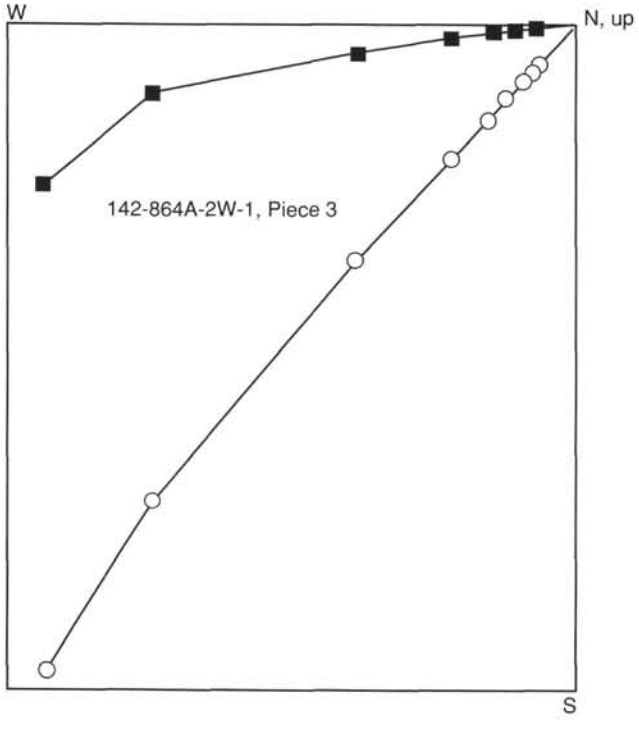

Figure 15. Zijderveld plot showing the changes in the orthogonal components of the NRM of Sample 142-864A-2W-1, Piece 3, with increasing alternating field steps between 0 and 70 mT. The direction (North, up) is of no significance for an unoriented sample.

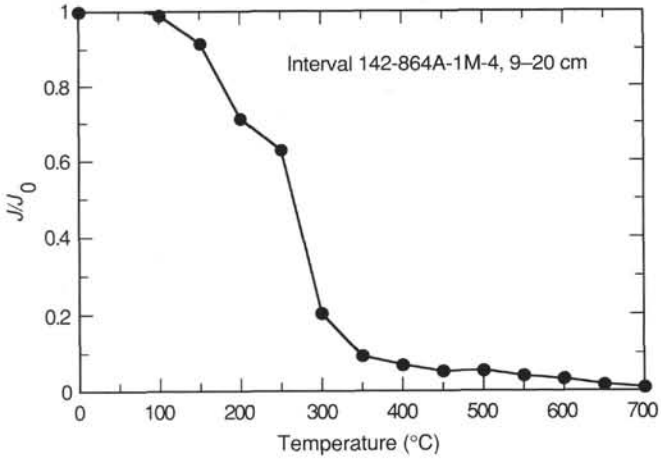

Figure 17. Changes in the remanent magnetization intensity during thermal demagnetization of samples.

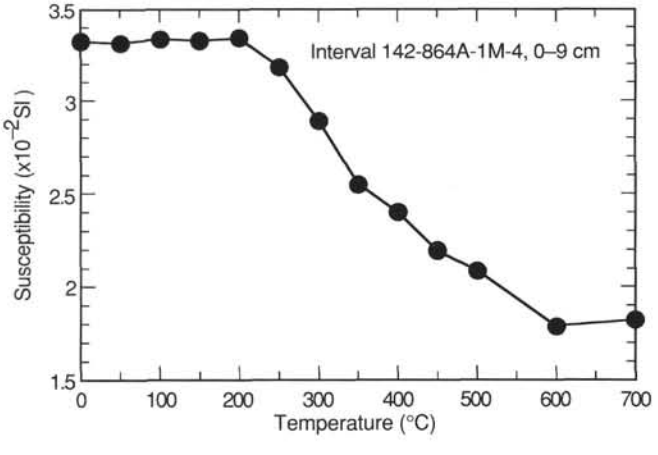

Figure 18. Changes in the magnetic susceptibility of a sample during the thermal treatment in a field-free space.